Multidimensional aware Riemann solver for the Eulerian droplet equation system

Heloise Beaugendre, Agnes Chan, Gérard Gallice, Raphaël Loubère, Pierre-Henri Maire, François Morency, Thomas Vigier

Eleventh International Conference on Computational Fluid Dynamics (ICCFD11), Maui, HI, USA, July 11-15, 2022

ICCFD11-2022-4101

Multidimensional aware Riemann solver for the Eulerian droplet equation system

H. Beaugendre*, A. Chan*,**, G. Gallice**, R. Loubère*, P.H. Maire**, F. Morency ***and T. Vigier*
Corresponding author: heloise.beaugendre@math.u-bordeaux.fr

* IMB, Université de Bordeaux, CNRS UMR 5251, Bordeaux INP and INRIA, F-33400 Talence, France.
** CEA Cesta, 15 Avenue des Sablières CS60001 33116, Le Barp cedex, France.
*** Mechanical Engineering Department, Ecole de technologie supérieure, Montréal, Canada.

Abstract: In clouds and under cold weather, water droplets impact and freeze on aircraft structures. The Eulerian model for the air-droplet flow predicts the droplet impingement. The model equations are close to the Euler equations but without a pressure term. Consequently, the resulting system is weakly hyperbolic and standard Riemann solvers cannot be used. To circumvent this problem, the system is modified to include the divergence of a particle pressure. The main purpose of this work is to implement a multidimensional HLLC Riemann solver for the modified formulation of the Eulerian droplet model. The method should preserve physical properties such as the density positivity and must produce accurate results compared to existing codes.

Keywords: Multi-phase flow, Pressureless Euler equations, Riemann solver, In-flight icing.

1 Introduction

In-flight icing still causes many crashes and accidents, as much as 8% of regional aircraft deathly accident [1]. Ice accretion on aircraft lifting structures induces a drag increase, a loss of lift, and a reduction of the stall angle [2]. This performance degradation, especially if sudden, is the cause of many accidents [3]. Ice accretion can also occur on engine air intakes, spinners and inlet fan blades. Frozen fan blades induce overload and unbalanced mass that would degrade the engine immediately. When this ice breaks away, and is ingested through the reminder of the propulsion system (engine and nacelle), it creates multiple damages. These damages have a serious negative impact on the operations costs and may also generate some incident concern [4, 5]. To minimize ice accretion, wings and propulsion systems have Ice Protection Systems (IPS) which mostly use air-heated technology through engine bled offs [6, 7]. Air-heated IPS carry associated design penalties and have themselves performance issues. If manufacturers use too cautious design margins, it leads to conservative non-optimized solutions.

The conception of aircraft IPS requires the prediction of areas impacted in-flight by cloud droplets. Critical aircraft surfaces where droplets impinge are prone to aircraft icing and must be protected. In clouds, the airflow around the wing transports suspended water droplets. Due to their high inertia, they impact aircraft surfaces and may freeze. The two-phase flow in this situation can be modelled using a one-way coupling algorithm since the droplet effects on the airflow is negligible because of the low water content [8, 9]. Indeed, the bulk density of the droplets over the bulk density of air is of the order of 10^{-3} in icing conditions. Generally, a one-way coupling models well a loading smaller than 0.1 [9].

For droplet diameters smaller than $100\mu m$, many works investigated the equation for droplet motion in airflow [10] . The spherical drag coefficient links the droplet momentum to the airflow. The gravity force can also be involved in large droplets or low air velocity flows. Early numerical codes use a Lagrangian

coordinate system attached to the droplet [11]. Instead, the CFD codes use an Eulerian coordinate system to solve for the droplet velocity $\mathbf{u}$ and the volume fraction of water (α) [9, 12, 13]. Compared to the Lagragian method, the Eulerian method does not make a priory estimate on the location of the impingement region and enables the identification of shadow areas [14]. In the shadow areas downstream of the aircraft, the droplets vanish. However, for simple cases, the calculation cost of the Eulerian method is higher when compared to the Lagrangian method. Still, high order implicit solvers, at least second order, enabling large CFL numbers can reduce the computational efforts.

The Eulerian droplet equation system is a particular form of the pressureless gas equations. The pressureless gas equations are often used to model clouds of dust [15, 16], with ρ the dust density and $\mathbf{u}$ the velocity. The pressureless gas equations are weakly hyperbolic and the Jacobian matrix is not diagonalizable. The development of delta-shocks, and the emergence of the vacuum state characterize this weakly hyperbolic system.

First order and second order schemes are developed to solve the pressureless gas, such as the schemes based on the kinetic approximations [17], the relaxation methods [18], or central schemes [19]. Recently, [20, 21] used the theory of Jordan canonical forms to solve the weakly hyperbolic systems and derive an upwind scheme. The addition of a perturbation parameter ϵ transforms the system in a strictly hyperbolic one, enabling the use of Riemann solvers, such as the Roe solver [22]. The perturbation parameter is equivalent to a particle pressure [23] with the pressure proportional to the density, $p = a^2\rho$. If the sound speed vanishes, $a \to 0$, then the pressureless system is recovered. [24] applied an idea developed originally in computational magnetohydrodynamics (MHD) [25]. Starting with the Eulerian droplet momentum equations, they add and substract a vector term involving the divergence of a particle pressure. Next, they split the system between a strictly hyperbolic part and a source term. They suggest a HLLC approximate Riemann solver that satisfied the positivity condition for the liquid water content. But once the Eulerian droplet equations are converted into a strictly hyperbolic system, one can use any standard Riemann solvers, such as the Roe solver, the HLLC solver or the HLLC-AUSM solver, as recently studied by [26].

Recent works have led to the development of a new Riemann solver[27, 28]. This solver is of the HLLC type and authors derive it from a Lagrangian framework. In this solver, the face flux is divided into two sub-face fluxes. The sub-face flux, related to a node, depends not only on the two states next to the sub-face but also on the nodal velocity. This nodal velocity is computed using all states surrounding the node, hence the name multi-dimensional aware flux. In the context of gas dynamics, the multi-point scheme shows good performance in suppressing numerical instabilities like even-odd decoupling and shock instabilities like carbuncles. Thanks to its positivity preserving property, we expect more robustness than from classic solvers.

In this work, the Eulerian droplet equations are modified according to Jung and Myong technique [24]. The objective is to investigate a new Godunov type Finite Volume scheme with multidimensional aware Riemann solvers: the multi-point Riemann solver. First, the Eulerian droplet equation system is derived from the force balance over a single droplet. Then, the equations are modified to obtain a hyperbolic system. Second, the general description of the multi-point Riemann solver is given in the context of gas dynamics. Third, the algorithm used to iteratively solve the pressureless system of equations is detailed, before some numerical results are presented.

2 Problem Statement

Inside a cloud, the compressible air and small liquid droplets flow around aircraft parts. Because the liquid water content is small, the effect of the droplets on the airflow is neglected. The flow is modelled as a two-phase flow with one way coupling.

The momentum equations compute the velocity (u, v) of spherical droplets. As illustrated on Figure 1, the droplets with diameter D and density ρ_w are carried by the airflow of density ρ_a and viscosity μ. The air velocity (u_a, v_a) creates a drag force $\mathbf{F_D}$ parallel to the relative velocity vector $((u_a - u), (v_a - v))$. The gravity force g also acts on the droplet. These two forces accelerate the droplet such that it reaches a velocity (u, v) at time t.

The Eulerian droplet equations consist of a mass conservation equation for the liquid water content, $\rho = \alpha$, and momentum conservation equations for the droplet velocity $\mathbf{u}$. The momentum equations do include source terms for the drag force exerted by the air

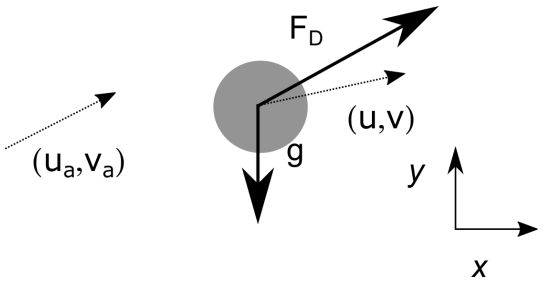

Figure 1: Forces on a droplet in an airflow

$$\mathbf{F_D} = (A_u(u_a - u), A_v(v_a - v)) \tag{1}$$

The drag coefficients A_u and A_v are the same in both directions

$$A_u = A_v = \frac{0.75\rho C_D Re\mu}{\rho_w D^2} \tag{2}$$

$$Re = \frac{\rho_a D}{\mu}\sqrt{(u_a - u)^2 + (v_a - v)^2} \tag{3}$$

The drag coefficient is adapted from [10]

$$C_D = \begin{cases} \frac{24}{Re}(1.0 + 0.15Re^{0.687}); & \text{if} \quad Re \leq 1300 \\ 0.4 & \text{if} \quad Re > 1300 \end{cases} \tag{4}$$

The droplets behave as a pressureless gas. Unless the calculation requires droplet temperature, the system does not define the energy equation. For the 2D pressureless equations, the conservative variables and the fluxes are:

$$\mathbf{U} = \begin{pmatrix} \rho \\ \rho u \\ \rho v \\ \rho \psi \end{pmatrix} \quad \mathbf{F} = \begin{pmatrix} \rho \mathbf{u_n} \\ \rho u \mathbf{u_n} \\ \rho v \mathbf{u_n} \\ \rho \mathbf{u_n} \psi \end{pmatrix} \quad \mathbf{Q} = \begin{pmatrix} 0 \\ A_u(u_a - u) \\ A_v(v_a - v) + \rho g(1 - \rho_a/\rho_w) \\ 0 \end{pmatrix} \tag{5}$$

where $A_u(u_a - u)$ and $A_v(v_a - v)$ stand for the aerodynamic drag in x and y direction. The contravariant velocity is $\mathbf{u_n} = \mathbf{u} \cdot \mathbf{n}$ with $\mathbf{n}$ the outward-pointing normal vector of the face. The buoyancy force definition $\rho g(1 - \rho_a/\rho_w)$ assumes the gravity vector point toward the negative y direction.

The convective part of the Eulerian droplet equations is not strictly hyperbolic. The classical Riemann solvers only apply to strictly hyperbolic systems of equation. Therefore, they cannot solve the unmodified system. One way to circumvent this problem is to modify the system by adding an artificial pressure term on both sides of the equations [29].

2.1 Modified pressureless equations

First, the general finite volume equation for non viscous flows is modified and written as

$$\frac{\partial}{\partial t}\int_\Omega \mathbf{U} d\Omega + \oint_{\partial\Omega} \mathbf{F} dS = \int_\Omega \mathbf{Q} d\Omega + \oint_{\partial\Omega} \mathbf{F_p} dS, \tag{6}$$

on a computational domain Ω. The conservative variables and the fluxes are now given by

$$\mathbf{U} = \begin{pmatrix} \rho \\ \rho u \\ \rho v \\ \rho \psi \end{pmatrix} \quad \mathbf{F} = \begin{pmatrix} \rho \mathbf{u_n} \\ \rho u \mathbf{u_n} + p n_x \\ \rho v \mathbf{u_n} + p n_y \\ \rho \mathbf{u_n} \psi \end{pmatrix}, \tag{7}$$

and the source terms by

$$\mathbf{F_p} = \begin{pmatrix} 0 \\ p n_x \\ p n_y \\ 0 \end{pmatrix} \quad \mathbf{Q} = \begin{pmatrix} 0 \\ A_u(u_a - u) \\ A_v(v_a - v) + \rho g(1 - \rho_a/\rho_w) \\ 0 \end{pmatrix}. \tag{8}$$

The artificial pressure p is related to the liquid water content, ρ, the gravity magnitude, g, and a reference droplet diameter d as

$$p = \rho g d. \tag{9}$$

The idea is to have an artificial pressure term equivalent to a classical pressure, $p \propto \rho$, for continuous compressible fluid. Specifically, for isothermal Euler equations, $p = a^2\rho$, where a is the speed of sound. Here, $a = \sqrt{gd}$.

The first and second terms, equation (7), on the left-hand side of equation (6) are strictly hyperbolic and consequently numerical methods can use Riemann solvers.

2.2 Boundary conditions

At farfield, inlet or outlet supersonic boundary conditions are imposed, taking into account that the speed of sound linked to the artificial pressure $a = \sqrt{gd}$ should be small.

A special boundary condition is imposed at the solid surface. The flow can leave the computational domain but it cannot enter. The projection of the velocity vector on the surface normal vector is first computed. If the flow leaves the computational domain, supersonic outlet boundary conditions are imposed. If the flow enters the computational domain, i.e. the droplets are ejected from the wall, a supersonic inlet is imposed with the conservative variables set to zero. Then,

$$\mathbf{U_{wall}} = \begin{cases} 0 & \text{if} \quad \mathbf{u_n} > 0 \\ \mathbf{U} & \text{if} \quad \mathbf{u_n} \leq 0 \end{cases} \tag{10}$$

3 New Godunov type Finite Volume scheme with multidimensional aware Riemann solver

This numerical method is inspired from the seminal work of G. Gallice [30] which has been recently pursued in [31] in 1D and [27] in 2D. This solver is a particular Finite Volume (FV) scheme for hyperbolic system of conservation laws, possibly with source terms. It uses a new vertex based Riemann Solver (RS) in such a way that all surrounding neighbour cells participate to the update of the current one.

Several classical and well adopted techniques have been revamped. First the FV scheme is written in a non-conservative way to allow for discontinuous fluxes across half-edges. Conservation is, however, retrieved by solving for the vertex based flux jumps. Although not classic, this approach has the main advantage to couple all neighbour cells regardless the mesh structure or the cell type. Second the RS, which is of 'HLLC type' [32], is derived from the Lagrangian framework [30] and further expressed in the Eulerian one by a Lagrange-to-Euler mapping. As such the properties of the Lagrangian RD are naturally inherited by the Eulerian one: consistency, positivity preservation, entropy dissipation and wave ordering [27] with a well-defined time-step control. Third this new FV scheme seems insensitive to spurious oscillatory phenomena sometimes encountered such as the carbuncle phenomena [33, 34].

In this section we will recall the main characteristics of this new Godunov type FV scheme with multi-dimensional aware RS. This scheme is referred as the 'Multi-point' solver. We will also point the differences

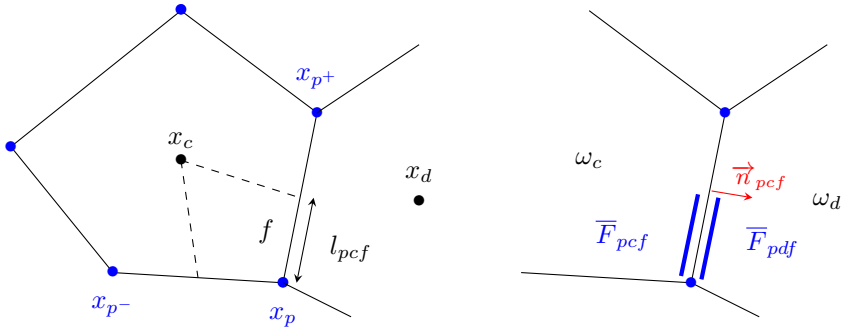

Figure 2: Sketch of a generic cell. Left: polygonal cell ω_c. Right: half interface between cell ω_c and cell ω_d

with a classical FV scheme using the HLLC RS which we refer to as a 'two-point' solver.

3.1 Multidimensional aware FV scheme for gas dynamics

First let us consider the 2D isothermal Euler equations with the equation of state $p = K\rho^\gamma$ with $K = gd$ is a constant and $\gamma = 1$, for which the sound speed is given by $a^2 = K\rho$ which consists of the homogeneous system (6)

$$\frac{\partial}{\partial t}\int_\Omega \mathbf{U} d\Omega + \oint_{\partial\Omega} \mathbf{F} dS = \mathbf{0}. \tag{11}$$

Notice that the last equation of (11) correspond to the advection of a passive tracer $0 \leq \psi \leq 1$. The computational domain Ω is a polygon covered by non-overlapping polygonal cells ω_c. c is the generic label of the cell. $\mathcal{P}(c)$ is the set of vertices (points) of ω_c. The generic label of a point is p and $\mathbf{x}_p$ denotes its vector position. The points of the cell ω_c are counter-clockwise ordered, and p^- and p^+ are respectively the previous and the next points with respect to p, see figure 2. The sub-cell ω_{pc} is the quadrangle formed by joining the cell center, $\mathbf{x}_c$, to the midpoints of $[\mathbf{x}_{p^-}, \mathbf{x}_p]$, $[\mathbf{x}_p, \mathbf{x}_{p^+}]$ and to $\mathbf{x}_p$. The set of sub-cells ω_{pc} for $p \in \mathcal{P}(c)$ constitutes a partition of the cell ω_c, that is, $\omega_c = \bigcup_{p\in\mathcal{P}(c)} \omega_{pc}$. The set of faces of the cell ω_c is denoted by $\mathcal{F}(c)$. Each face f of the cell c is decomposed into sub-faces (half-faces) by means of the partition of c induced by the sub-cells pc for $p \in \mathcal{P}(c)$. Doing so, we define $\mathcal{SF}(pc)$ the set of sub-faces attached to the corner pc. We denote respectively by l_{pcf} and $\mathbf{n}_{pcf} = (n_x, n_y)_{pcf}$ the measure and the unit outward normal of the sub-face f. We observe that the set of sub-faces $\mathcal{SF}(pc)$ for $p \in \mathcal{P}(c)$ constitutes a partition of the set of faces of ω_c, that is, $\mathcal{F}(c) = \bigcup_{p\in\mathcal{P}(c)} \mathcal{SF}(pc)$. Given a cell c and one of its faces f, the unique 'neighbour' cell associated is $d(c, f)$ or simply d to shorten the notation. The set of neighbours of the cell c is called $\mathcal{N}(c)$ and it will be more appropriately defined, either faced-based or node-based.

At last, any vector can be projected onto the canonical or normal/tangent $\mathbf{n}/\mathbf{t}$ base to a face f as:

$$\mathbf{u} = u\mathbf{e}_x + v\mathbf{e}_y = u_\mathbf{n}\mathbf{n} + u_\mathbf{t}\mathbf{t}, \quad \text{with} \quad u_\mathbf{n} = \mathbf{u}\cdot\mathbf{n}, \quad \text{and} \quad u_\mathbf{t} = \mathbf{u} - \mathbf{u}\cdot\mathbf{n}, \tag{12}$$

$$\mathbf{x} = x\mathbf{e}_x + y\mathbf{e}_y = x_\mathbf{n}\mathbf{n} + x_\mathbf{t}\mathbf{t}, \quad \text{with} \quad x_\mathbf{n} = \mathbf{x}\cdot\mathbf{n}, \quad \text{and} \quad x_\mathbf{t} = \mathbf{x} - \mathbf{x}\cdot\mathbf{n}, \tag{13}$$

Integrating the system (11) over ω_c yields

$$|\omega_c|\frac{d\mathbf{U}_c}{dt} + \int_{\partial\omega_c} \mathbf{F}(\mathbf{U})\mathbf{n}\, ds = \mathbf{0}, \tag{14}$$

where $\mathbf{U}_c(t) = \dfrac{1}{|\omega_c|}\displaystyle\int_{\omega_c} \mathbf{U}(\mathbf{x}, t)\, dv$ is the cell-averaged value of $\mathbf{U}$ over ω_c and $\mathbf{U}_c^n \equiv \mathbf{U}_c(t^n)$ for any discrete time t^n. Employing a classical first-order explicit time integration turns (14) into

$$\mathbf{U}_c^{n+1} - \mathbf{U}_c^n + \frac{\Delta t}{|\omega_c|}\int_{\partial\omega_c} \mathbf{F}(\mathbf{U}^n)\mathbf{n}\, ds = \mathbf{0}. \tag{15}$$

The Finite Volume scheme (14) requires the construction of an approximation of the normal flux integral. Following [27] we design an original node-based approximation of this integral term relying on the partition of ω_c into sub-cells as

$$\int_{\partial\omega_c} \mathbf{F}(\mathbf{U}^n)\mathbf{n}\, ds = \sum_{p\in\mathcal{P}(c)} \int_{\partial\omega_{pc}\cap\partial\omega_c} \mathbf{F}(\mathbf{U}^n)\mathbf{n}\, ds \simeq \sum_{f\in\mathcal{SF}(pc)} l_{pcf}\overline{\mathbf{F}}_{pcf} \tag{16}$$

where the surface integral term in the middle term is approximated along the sub-faces by means of the sub-face flux related to f attached to the corner pc, denoted $\overline{\mathbf{F}}_{pcf}$.
Substituting the above forms into (15) yields the sub-face-based generic Finite Volume scheme

$$\mathbf{U}_c^{n+1} - \mathbf{U}_c^n + \frac{\Delta t}{|\omega_c|} \sum_{p\in\mathcal{P}(c)} \sum_{f\in\mathcal{SF}(pc)} l_{pcf}\overline{\mathbf{F}}_{pcf} = \mathbf{0}, \tag{17}$$

entirely characterized by the sub-face flux $\overline{\mathbf{F}}_{pcf}$.

Simple Lagrangian/Eulerian Riemann Solvers. A simple generic Eulerian Riemann solver considers constant intermediate states $\mathbf{U}^\star_{c/d}$ separated by simple waves, therefore given by constant wave speeds Λ_c, Λ_0 and Λ_d, which in our case are deduced from their Lagrangian counterparts $-\lambda_c \le \lambda_0 = 0 \le \lambda_d$ as

$$\Lambda_c = u_{\mathbf{n},c} - \lambda_c \frac{1}{\rho_c} = u^\star_{\mathbf{n}} - \lambda_c \frac{1}{\rho^\star_c}, \quad \Lambda_0 = u^\star_{\mathbf{n}}, \quad \Lambda_d = u^\star_{\mathbf{n}} + \lambda_d \frac{1}{\rho^\star_d} = u_{\mathbf{n},d} + \lambda_d \frac{1}{\rho_d}. \tag{18}$$

If the Lagrangian approximate Riemann solver preserves the positivity of specific volumes with large enough wave speeds, *i.e.*, $\dfrac{1}{\rho^\star_S} \ge 0$, then these Eulerian wave speeds are ordered: $\Lambda_c \le \Lambda_0 \le \Lambda_d$. In [27], it is shown that the positivity holds true granted that the Lagrangian wave speeds satisfy an explicit condition on the star velocity. The Lagrangian and Eulerian simple approximate Riemann solvers operating over two states called left and right respectively associated to the cell c and d in the direction $\mathbf{n}_{pcf}$, are given by (m is the constant Lagrangian mass)

$$\mathbf{W}_L\left(\mathbf{V}_c, \mathbf{V}_d, \frac{m}{t}\right) = \begin{cases} \mathbf{V}_c & \text{if } \frac{m}{t} \le -\lambda_c, \\ \mathbf{V}^\star_c & \text{if } -\lambda_c < \frac{m}{t} \le 0, \\ \mathbf{V}^\star_d & \text{if } 0 < \frac{m}{t} \le \lambda_d, \\ \mathbf{V}_d & \text{if } \lambda_d < \frac{m}{t}. \end{cases} \quad \mathbf{W}_E\left(\mathbf{U}_c, \mathbf{U}_d, \frac{x_\mathbf{n}}{t}\right) = \begin{cases} \mathbf{U}_c & \text{if } \frac{x_\mathbf{n}}{t} \le \Lambda_c, \\ \mathbf{U}^\star_c = \mathbf{U}(\mathbf{V}^\star_c) & \text{if } \Lambda_c < \frac{x_\mathbf{n}}{t} \le \Lambda_0, \\ \mathbf{U}^\star_d = \mathbf{U}(\mathbf{V}^\star_d) & \text{if } \Lambda_0 < \frac{x_\mathbf{n}}{t} \le \Lambda_d, \\ \mathbf{U}_d & \text{if } \Lambda_d < \frac{x_\mathbf{n}}{t}. \end{cases} \tag{19}$$

Here, $\mathbf{V} \mapsto \mathbf{U}(\mathbf{V})$ is the Lagrange-to-Euler mapping defined by $\mathbf{V} = \dfrac{1}{\rho}(\mathbf{U} - \rho\mathbf{e}_x) + \dfrac{1}{\rho}\mathbf{e}_x$, where $\mathbf{e}_x = (1,0)^t$ [30, 27]. The Eulerian intermediate states read $\mathbf{U}^\star_S = (\rho^\star_S, \rho^\star_S u^\star_\mathbf{n}, \rho^\star_S u^\star_{\mathbf{t},S}, \rho^\star_S e^\star_S)^t$ are deduced from their Lagrangian counterpart $\mathbf{V}^\star_S = (1/\rho^\star_S, u^\star_\mathbf{n}, u^\star_{\mathbf{t},S}, e^\star_S)^t$ for $S = c, d$, check [30, 27] for more details. Following the derivation in [27], we observe that the simple Riemann solvers are parameterized by the normal star-velocity $u^\star_\mathbf{n}$ and the intermediate states of $\mathbf{W}_L$ read

$$\frac{1}{\rho^\star_c} = \frac{1}{\rho_c} + \frac{u^\star_\mathbf{n} - u_{\mathbf{n},c}}{\lambda_c}, \quad \frac{1}{\rho^\star_d} = \frac{1}{\rho_d} - \frac{u^\star_\mathbf{n} - u_{\mathbf{n},d}}{\lambda_d}, \quad u^\star_{\mathbf{t},c} = u_{\mathbf{t},c}, \quad u^\star_{\mathbf{t},d} = u_{\mathbf{t},d}, \tag{20}$$

$$e^\star_{c/d} = \varepsilon_{c/d} - p_{c/d}\left(\frac{1}{\rho^\star_{c/d}} - \frac{1}{\rho_{c/d}}\right) + \frac{\lambda_{c/d}}{2}\left(\frac{1}{\rho^\star_{c/d}} - \frac{1}{\rho_{c/d}}\right)^2 + \frac{1}{2}\left((u^\star_\mathbf{n})^2 + (u_{\mathbf{t},c})^2\right),$$

where $\varepsilon_{c/d} = e_{c/d} - \dfrac{1}{2}\left(u^2_{c/d} + v^2_{c/d}\right)$. The Lagrangian wave speeds $-\lambda_c$, λ_0 and λ_d are ordered by construction and must be large enough to ensure positivity preservation, for instance by fulfilling [27]

$$\lambda_c \ge \max\left(\rho_c a_c, -\rho_c(u^\star_\mathbf{n} - u_{\mathbf{n},c})\right), \quad \lambda_d \ge \max\left(\rho_d a_d, \rho_d(u^\star_\mathbf{n} - u_{\mathbf{n},d})\right). \tag{21}$$

By construction, the Eulerian approximate Riemann solver $\mathbf{W}_E$ inherits the same properties as its Lagrangian counterpart (positivity preservation, entropy production, wave ordering). Notice that in the previous equations, the only remaining unknown is $u^\star_{\mathbf{n}}$. Here we make the fundamental assumption that a unique nodal velocity exists $\mathbf{u}_p$ such that $\mathbf{u}_p \cdot \mathbf{n}_{pcf} = u^\star_{\mathbf{n}}$ for any face f impinging at the node p. Notice that with such an assumption, $\mathbf{u}_p$ is shared by all faces/cells around p. This nodal velocity is a central key for our solver.

Multi-dimensional aware numerical flux. Taking into account the Eulerian RS (derived from its Lagrangian counterpart), our non classical Eulerian numerical flux finally reads

$$\begin{aligned}\overline{\mathbf{F}}_{\mathbf{n}_{pcf}} = \frac{1}{2}\left[\mathbf{F}_{\mathbf{n}_{pcf}}(\mathbf{U}_c) + \mathbf{F}_{\mathbf{n}_{pcf}}(\mathbf{U}_d)\right] \quad &- \quad \frac{1}{2}\Big[|\Lambda_c|(\mathbf{U}^\star_c - \mathbf{U}_c) + |\Lambda_0|(\mathbf{U}^\star_d - \mathbf{U}^\star_c) + |\Lambda_d|(\mathbf{U}_d - \mathbf{U}^\star_d)\Big] \\ &- \quad \frac{\lambda_c + \lambda_d}{2}\left[\mathbf{u}_p \cdot \mathbf{n}_{pcf} - \overline{u}_{\mathbf{n}_{pcf}}\right](0, 1, 0, \mathbf{u}_p \cdot \mathbf{n}_{pcf})^t. \end{aligned} \tag{22}$$

Here the Godunov "acoustic" mean velocity $\overline{u}_{\mathbf{n}_{pcf}}$ is given by the expression

$$\overline{u}_{\mathbf{n}_{pcf}} = \frac{\lambda_c \mathbf{u}_c \cdot \mathbf{n}_{pcf} + \lambda_d \mathbf{u}_d \cdot \mathbf{n}_{pcf}}{\lambda_c + \lambda_d} - \frac{p_d - p_c}{\lambda_c + \lambda_d}. \tag{23}$$

The extra-term in (22) only appears for the momentum and energy equations. It is easy to recognize that a classical (two points) numerical flux is retrieved when one set $\mathbf{u}_p \cdot \mathbf{n}_{pcf} = \overline{u}_{\mathbf{n}_{pcf}}$ because the last term in (22) cancels out. In this only case, the flux is the same at the face f for cell c and d but applied with a plus (resp. a minus) sign in the cell c (resp. d). The conservation is simply obtained because there is no flux jump at the interface between neighbour cells. However there is no reason *a priori* that a unique nodal velocity $\mathbf{u}_p$ exists to fulfill this requirement.
Contrarily in our approach we accept that $\mathbf{u}_p \cdot \mathbf{n}_{pcf} \neq \overline{u}_{\mathbf{n}_{pcf}}$. As such the numerical flux depends not only on the two states adjacent to the sub-face but also on all states surrounding node p through the expression of the nodal velocity $\mathbf{u}_p$. Hence the name multi-point or multidimensional aware flux.

Nodal solver. The last unknown in the previous flux is the nodal velocity $\mathbf{u}_p$ which one computes by invoking local conservation around the node p [31, 27]. Indeed the interface jumps must sum to zero for conservation purposes that is

$$\sum_{f \in \mathcal{SF}(p)} l_{pcf}(\lambda_c + \lambda_d)(\mathbf{u}_p \cdot \mathbf{n}_{pcf} - \overline{u}_{\mathbf{n}_{pcf}})\mathbf{n}_{pcf} = \mathbf{0}, \tag{24}$$

where f is the sub-face in-between cells c and d in contact with the point p. This boils down to express (24) as a linear system $\mathbb{M}_p\, \mathbf{u}_p = \mathbf{w}_p$, where $\mathbf{u}_p$ is the unknown and

$$\mathbb{M}_p = \sum_{f \in \mathcal{SF}(p)} l_{pcf}(\lambda_c + \lambda_d)(\mathbf{n}_{pcf} \otimes \mathbf{n}_{pcf}), \qquad \mathbf{w}_p = \sum_{f \in \mathcal{SF}(p)} l_{pcf}(\lambda_c + \lambda_d)\overline{u}_{\mathbf{n}_{pcf}}\mathbf{n}_{pcf}. \tag{25}$$

This system, called a 'nodal solver', always admits a unique solution which provides the nodal velocity $\mathbf{u}_p$, given physical states and wave speeds for all faces impinging at the current node. Once $\mathbf{u}_p$ is computed, then we can get $\overline{u}_{\mathbf{n}_{pcf}} = \mathbf{u}_p \cdot \mathbf{n}_{pcf}$, the wave speeds, the intermediate states, the flux (22), and finally the new mean values from the FV scheme (17). The foregoing system has been already obtained when constructing a cell-centered FV discretization of multidimensional Lagrangian hydrodynamics [35], also retrieved in [36, 27] for designing an Eulerian FV scheme.

Time-step condition. Omitting the details (see [27]) the practical time step condition writes

$$\Delta t \leq \frac{|\omega_c|}{\displaystyle\sum_{p \in \mathcal{P}(c)} \sum_{f \in \mathcal{SF}(pc)} l_{pcf}\left(|\mathbf{v}^n_c \cdot \mathbf{n}_{pcf}| + \frac{\lambda_c}{\rho^n_c}\right)}. \tag{26}$$

Second-order extension. The second-order extension of the previous FV scheme is obtained by piecewise reconstruction of primitive variables supplemented with minmod or Ventakakrishnan slope limiters in space and Strong Stability Preserving Runge-Kutta scheme in time, see [35] for the second-order extension for Lagrangian FV scheme. The first-order and second-order versions of the scheme have been validated for gas dynamics [31, 27] and shallow water equations [37], in 1D [31], 2D [27] and 3D [28].

4 Algorithm for pressureless system of equations

In order to solve the pressureless system of equations one must adapt the previous solver. First, the energy equation for gas-dynamics is useless for the pressureless model as the pressure only depends on the density. Second, an extra equation for a passive convected scalar variable Ψ is added. For the first-order explicit scheme it yields

$$(\rho\Psi)_c^{n+1} = (\rho\Psi)_c^n - \frac{\Delta t}{|\omega_c|} \sum_{f\in\mathcal{F}(c)} l_f \, (\rho\Psi)_f \mathbf{u}_f \cdot \mathbf{n}_{cf}, \tag{27}$$

where $\mathbf{u}_f = \dfrac{\mathbf{u}_p + \mathbf{u}_{p+1}}{2}$ with points p and $p+1$ being the two end-points of face f. Moreover $(\rho\Psi)_f$ is equal to $\rho_c\Psi_c$ (resp. $\rho_d\Psi_d$) if $\mathbf{u}_f \cdot \mathbf{n}_{cf} \geq 0$ (resp. < 0). Notice that we have reused the nodal velocity $\mathbf{u}_p$ which are in reality a good approximation of the material velocity.
Third the source terms in (8) are easily taken into account. $\mathbf{F_p}$ is simply discretized as

$$\int_{\omega_c} \mathbf{F_p}(\mathbf{U})\, dv = \int_{\partial\omega_c} p\mathbf{n}\, ds = \sum_{f\in\mathcal{F}(c)} l_f p_f \mathbf{n}_f, \tag{28}$$

where $p_f = (\rho_f)gd$ and ρ_f is given by the Riemann solver, that is either ρ_L, $\rho_L^\star$, $\rho_R^\star$ or ρ_R depending on the wave speeds, see (19).

On the other hand $\mathbf{Q}$ is nothing but a reaction term which at first and second orders in space can be approximated as

$$\int_{\omega_c} \mathbf{Q}(\mathbf{U})\, dv = |\omega_c| \begin{pmatrix} 0 \\ (A_u)_c(u_{a,c} - u_c^n) \\ (A_v)_c(v_{a,c} - v_c^n) + \rho_c^n g(1 - \rho_{a,c}/\rho_w) \\ 0 \end{pmatrix}. \tag{29}$$

For the second order in time, the source terms are approximated once for the predictor and one more time for the corrector stage (the same if a RK scheme is employed).
This complete the description of the numerical method.

5 Numerical results

In this section we present a single test case to assess the numerical method. Notice that the numerical method has been already validated for gas dynamics and shallow-water systems of equations.

The flow of cloud droplets around a cylinder is studied to demonstrate the new solver capability. First, the Euler flow solution around a cylinder is computed, see figure 3. Farfield boundary conditions are imposed on the domain and slip wall boundary condition on the cylinder. The farfield temperature is set to 273.15 K, the pressure at 101325.0 Pa, and the Mach number at 0.2. Once the airflow solution is computed, the pressureless system is resolved. The droplet diameter is $40\mu m$ and the water density is $1000kg/m^3$. At farfield, the droplet velocity is equal to the air velocity and $\rho/\rho_{inf} = 1$. In our computations the reference droplet diameter that appears in the artificial pressure is equal to the droplet diameter. The droplet solution, figure 4 shows an increase in liquid water content on the cylinder front part. Also, very low-density region is visible on the back of the cylinder. In a narrow area close to the cylinder, the liquid water content goes from around one to around zero. Results are in agreement with literature, except for spurious oscillations

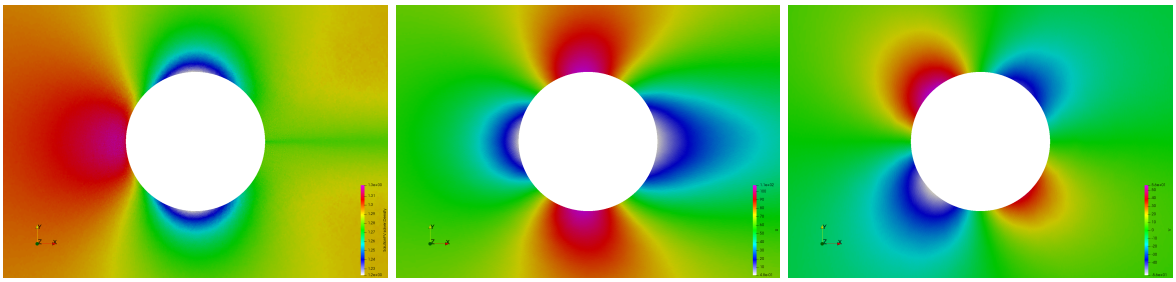

Figure 3: Euler flow solution around the cylinder, left: density; middle: u component of the velocity; right: v component of the velocity

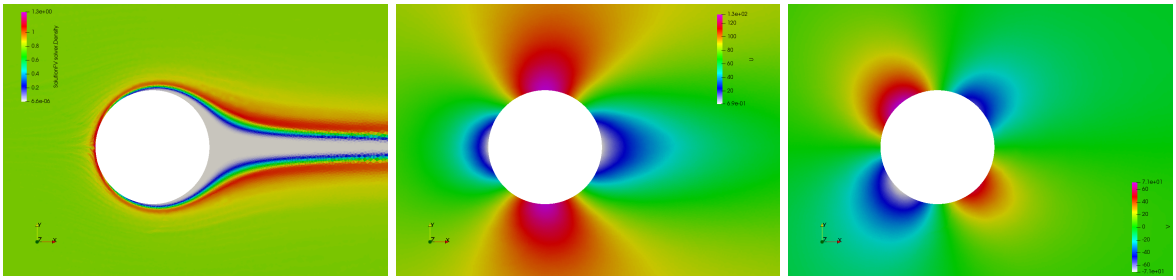

Figure 4: Pressureless flow solution around the cylinder, left: liquid water content; middle: u component of the droplet velocity; right: v component of the droplet velocity

on the liquid water content in front of the cylinder. These oscillations do not seem to change the solution anywhere other than on the front of the cylinder. Further investigations should be performed to understand the origin of these oscillations.

6 Conclusion and Perspectives

In this work, we investigate the multi-point Riemann solver adapted to solve water droplets flow. The two-phase flow is modelled using a one-way coupling. The obtained Eulerian droplet equations, a pressureless equation system, must be modified to obtain a hyperbolic system. A perturbation parameter equivalent to a pressure term is added on the left side and subtracted on the right side of the momentum equations. The multi-point solver is adapted to the pressureless system. A second order in time explicit scheme is used to march the solution toward the steady state. Preliminary results have been obtained around a cylinder. Further investigations should be performed to assess the capacities of the proposed scheme to solve the pressureless system.

References

[1] P. Appiah-Kubi, B. Martos, I. Atuahene, and S. William. U.S. inflight icing accidents and incidents, 2006 to 2010. In *IIE Annual Conference and Expo 2013*, 2013.

[2] M. B. Bragg, A. P. Broeren, and L. A. Blumenthal. Iced-airfoil aerodynamics. *Progress in Aerospace Sciences*, 41:323–362, 2005.

[3] Transportation Safety Board of Canada. Air transportation safety investigation report a17c0146. Report, Transportation Safety Board of Canada, October 2021.

[4] J. Mason, J. Strapp, and P. Chow. The ice particle threat to engines in flight. Report AIAA-2006-206, American Institute of Aeronautics and Astronautics, 2006.

[5] P. Veres Joseph and C. Jorgenson Philip. Modeling commercial turbofan engine icing risk with ice crystal ingestion. Technical Report AIAA-2013-2679, American Institute of Aeronautics and Astronautics, 2013.

[6] S. K. Thomas, R. P. Cassoni, and C. D. MacArthur. Aircraft anti-icing and de-icing techniques and modeling. *Journal of Aircraft*, 33(5):841–854, 1996.

[7] R. Hannat, J. Weiss, F. Garnier, and F. Morency. Application of the dual kriging method for the design of a hot-air-based aircraft wing anti- icing system. *Engineering Applications of Computational Fluid Mechanics*, 8(4):530–548, 2014.

[8] P. McComber and G. Touzot. Calculation of the impingement of cloud droplets in a cylinder by the finite-element method. *Journal of the Atmospheric Sciences*, 38:1027–1036, 1981.

[9] W. G. Bourgault, Y.and Habashi, J. Dompierre, and G. S. Baruzzi. A finite element method study of eulerian droplets impingement models. *International Journal of Numerical Methods in Fluids*, 29:429–449, 1999.

[10] R. Clift, J. R. Grace, and M. E. U. https books google ca books id UUrOmD niUQC Weber. *Bubbles, Drops, and Particles*. Dover Publications, 2005.

[11] William B. Wright. Validation results for lewice 3.0. Report AIAA Paper 2005-1243, American Institute of Aeronautics and Astronautics Inc., January 10 - January 13 2005.

[12] F. Capizzano and E. Iuliano. A eulerian method for water droplet impingement by means of an immersed boundary technique. *Journal of Fluids Engineering, Transactions of the ASME*, 136(4), 2014.

[13] I. Kim, N. Bachchan, and O. Peroomian. Supercooled large droplet modeling for aircraft icing using an eulerian-eulerian approach. *Journal of Aircraft*, 53(2):487–500, 2016.

[14] Morency F., Beaugendre H., and Habashi W. Fensap-ice : Effect of ice shapes on 3d eulerian droplet impingement. Technical Report AIAA-2003-1223, American Institute of Aeronautics and Astronautics, 2003.

[15] R. J. Leveque. The dynamics of pressureless dust clouds and delta waves. *Journal of Hyperbolic Differential Equations*, 1(2):315–327, 2004.

[16] S.-J. Paardekooper and G. Mellema. Dust flow in gas disks in the presence of embedded planets. *Astronomy & Astrophysics*, 453:1129–1140, 2006.

[17] F. Bouchut, Shi Jin, and Xiantao Li. Numerical approximations of pressureless and isothermal gas dynamics. *SIAM Journal of Numerical Analysis*, 41(1):135–158, 2003.

[18] Christophe Berthon, Michael Breuß, and Marc-Olivier Titeux. A relaxation scheme for the approximation of the pressureless euler equations. *Numerical Methods for Partial Differential Equations*, 22(2), 2006.

[19] Guang-Shan Jiang and Eitan Tadmor. Nonoscillatory central schemes for multidimensional hyperbolic conservation laws. *SIAM Journal on Scientific Computing*, 19(6):1892–1917, 1998.

[20] Naveen Kumar Garg, Michael Junk, S.V. Raghurama Rao, and M. Sekhar. An upwind method for genuine weakly hyperbolic systems. 2017.

[21] Naveen Kumar Garg. A class of upwind methods based on generalized eigenvectors for weakly hyperbolic systems. *Numerical Algorithms*, 83(3):1091–1121, 2020.

[22] Timothy A. Smith, David J. Petty, and Carlos Pantano. A roe-like numerical method for weakly hyperbolic systems of equations in conservation and non-conservation form. *Journal of Computational Physics*, 316:117–138, 2016.

[23] S. Keita and Y. Bourgault. Eulerian models with particle pressure for air-particle flows. *European Journal of Mechanics B-Fluids*, 78:263–275, 2019.

[24] S. K. Jung and R. S. Myong. A second-order positivity-preserving finite volume upwind scheme for air-mixed droplet flow in atmospheric icing. *Computers & Fluids*, 86:459–469, 2013.

[25] P. Janhunen. A positive conservative method for magnetohydrodynamics based on hll and roe methods. *Journal of Computational Physics*, 160(2):649–661, 2000.

[26] Omid Ejtehadi, Ehsan Mahravan, and Ilyoup Sohn. Investigation of shock and a dust cloud interaction in eulerian framework using a newly developed openfoam solver. *International Journal of Multiphase Flow*, 145:103812, 2021.

[27] G. Gallice, A. Chan, R. Loubère, and P.-H. Maire. Entropy stable and positivity preserving Godunov-type schemes for multidimensional hyperbolic systems on unstructured grid. *In revision Journal of Computational Physics*, 000:XXX–XXX, 2022.

[28] A. Chan, G. Gallice, R. Loubère, and P.-H. Maire. Revisiting riemann solvers in the lagrangian and

eulerian frameworks and their associated numerical methods in 3d. *preprint*, 2022.

[29] S. Keita and Y. Bourgault. Eulerian droplet model: Delta-shock waves and solution of the riemann problem. *Journal of Mathematical Analysis and Applications*, 472:1001–1027, 2019.

[30] G. Gallice. Positive and Entropy Stable Godunovov-Type Schemes for Gas Dynamics and MHD Equations in Lagrangian or Eulerian Coordinates. *Numer. Math.*, 94(4):673–713, 2003.

[31] A. Chan, G. Gallice, R. Loubère, and P.-H. Maire. Positivity preserving and entropy consistent approximate riemann solvers dedicated to the high-order MOOD-based finite volume discretization of lagrangian and eulerian gas dynamics. *Computers & Fluids*, 229:105056, 2021.

[32] E. F. Toro. *Riemann solvers and numerical methods for fluid dynamics : a practical introduction.* Springer-Verlag, Berlin, Allemagne, 2nd edition, 1999.

[33] M. Pandolfi and D. D'Ambrosio. Numerical Instabilities in Upwind Methods: Analysis and Cures for the Carbuncle Phenomenon. *Journal of Computational Physics*, 166(2):271–301, January 2001.

[34] A.V. Rodionov. Artificial viscosity Godunov-type schemes to cure the carbuncle phenomenon. *Journal of Computational Physics*, 345:308–329, 2017.

[35] P.-H. Maire. A high-order cell-centered Lagrangian scheme for two-dimensional compressible fluid flows on unstructured meshes. *Journal of Computational Physics*, 228:2391–2425, 2009.

[36] Z. Shen, W. Yan, and G. Yuan. A robust and contact resolving Riemann solver on unstructured mesh, Part I, Euler method. *Journal of Computational Physics*, 268:432–455, 2014.

[37] Agnes Chan, Gérard Gallice, Manuel J. Castro, Raphaël Loubère, and Pierre-Henri Maire. A well-balanced and positive finite volume scheme for Shallow-Water equations in multi-dimensions for unstructured grids derived from Lagrangian roots. 2022.